Chemistry–A European Journal

Research Article
doi.org/10.1002/chem.202104249

Chemistry
Europe
European Chemical
Societies Publishing

www.chemeurj.org

Redox Replacement of Silver on MOF-Derived Cu/C Nanoparticles on Gas Diffusion Electrodes for Electrocatalytic CO$_2$ Reduction

Nivedita Sikdar[+],[a] João R. C. Junqueira[+],[a] Denis Öhl,[a] Stefan Dieckhöfer,[a] Thomas Quast,[a] Michael Braun,[b] Harshitha B. Aiyappa,[a] Sabine Seisel,[a] Corina Andronescu,[b] and Wolfgang Schuhmann*[a]

Abstract: Bimetallic tandem catalysts have emerged as a promising strategy to locally increase the CO flux during electrochemical CO$_2$ reduction, so as to maximize the rate of conversion to C–C-coupled products. Considering this, a novel Cu/C–Ag nanostructured catalyst has been prepared by a redox replacement process, in which the ratio of the two metals can be tuned by the replacement time. An optimum Cu/Ag composition with similarly sized particles showed the highest CO$_2$ conversion to C$_{2+}$ products compared to non-Ag-modified gas-diffusion electrodes. Gas chromatography and in-situ Raman measurements in a CO$_2$ gas diffusion cell suggest the formation of top-bound linear adsorbed *CO followed by consumption of CO in the successive cascade steps, as evidenced by the increasing νC–H bands. These findings suggest that two mechanisms operate simultaneously towards the production of HCO$_2$H and C–C-coupled products on the Cu/Ag bimetallic surface.

Introduction

Electrochemical CO$_2$ reduction (CO$_2$RR) to sustainable fuels and carbon-based chemical production represents a route to alleviate overall fossil fuel consumption and mitigate the consequences of climate change.[1] Addressing solutions to a) technical challenges such as electrolyzer configuration, b) electrode fabrication, c) improvement of mass transport to regulate the local concentration of active reaction species,[2] and d) development of novel catalysts are in the focus of scientific interest. Among single-metal-based catalysts, copper is the only metal capable of generating high-value C–C-coupled hydrocarbons and alcohols.[3] In recent studies, a "tandem approach" with bimetallic systems, preferably with Cu (e.g., Au–Cu, Ag–Cu, Zn–Cu, Cu–Pd, Cu–Ga, Cu–Sn etc.) or composites (e.g., CoPc–Zn–N–C) have emerged as promising strategy to boost the formation of higher carbon-containing hydrocarbons during the CO$_2$RR.[4,5] In this consecutive process, CO$_2$ is initially reduced to CO followed by further reduction of surface adsorbed *CO intermediates into C$_{2+}$ hydrocarbons. The local CO concentration on a Cu surface exceeds the solubility limit by establishing the nonequilibrium state, which cannot be achieved by simply feeding in a CO$_2$/CO gas mixture.[6] Also, the local surface coverage of *CO intermediates on Cu metal tends to suppress the competitive hydrogen evolution reaction (HER) by reducing the effective number of electrocatalytically active HER sites due to weakening of the metal-bound H adsorption energy.[7] Among several possible compositions, coupled Cu–Ag systems enhance the CO$_2$RR selectivity towards C–C-coupled products by controlling the adsorption of the key intermediate CO on the catalyst surface.[8,9,10] Notably, a low Ag content is preferred as neighbouring Cu atom ensembles are pivotal for the desired C–C coupling into C$_{2+}$ products.[11] Although metallic Cu and Ag are thermodynamically immiscible at ambient conditions, past reports on Cu/Ag couples revealed that the catalyst synthesis routes could have a direct influence on the extent of metastable Cu/Ag alloying and other relevant catalytic properties.[9,10,12] Therefore, studying alternative Cu/Ag preparation methods to realize nonequilibrium miscibility between Cu and Ag, especially Cu–Ag interactions, might be promising to enhance the CO$_2$RR activity and selectivity, which can then be used to guide the future design of novel catalyst materials. Such bimetallic surfaces are additionally model systems to investigate cascade reaction through in-situ spectroscopic studies to understand the transition of surface adsorbed

[a] Dr. N. Sikdar,[+] J. R. C. Junqueira,[+] Dr. D. Öhl, S. Dieckhöfer, T. Quast, Dr. H. B. Aiyappa, Dr. S. Seisel, Prof. W. Schuhmann
Analytical Chemistry-Center for Electrochemical Sciences (CES)
Faculty of Chemistry and Biochemistry
Ruhr University Bochum
Universitätsstraße 150, 44780 Bochum (Germany)
E-mail: wolfgang.schuhmann@rub.de

[b] M. Braun, Prof. C. Andronescu
Chemical Technology III
Faculty of Chemistry and CENIDE Center for Nanointegration
University Duisburg-Essen
Carl-Benz Straße 199, 47057 Duisburg (Germany)

[+] These authors contributed equally to this work.

Chem. Eur. J. 2022, 28, e202104249 (1 of 9)

© 2022 The Authors. Chemistry - A European Journal published by Wiley-VCH GmbH

Chemistry–A European Journal

Research Article
doi.org/10.1002/chem.202104249

**Chemistry
Europe**
European Chemical
Societies Publishing

*CO intermediates into C_{2+} products, which is not sufficiently studied until now.[13–19] Moreover, the majority of the studies were performed in CO_2-saturated $KHCO_3$ solution, where the catalytic activity is limited by the mass transport of CO_2. In-situ studies are most relevant when performed in KOH as electrolyte in a gas diffusion cell, which motivated us to address this in this work.

Herein, electroless redox replacement, which is also known as galvanic replacement, was implemented as a straightforward strategy to synthesize Cu/Ag bimetallic catalysts directly on gas-diffusion electrodes (GDE) by atomically displacing Cu with the more noble metal Ag ($Ag^+/Ag^0 = 0.80$ V; $Cu^{2+}/Cu^0 = 0.34$ V vs. SHE).[20] Firstly, the Cu catalyst was synthesized in the form of metallic Cu nanoparticles (NP) coated with a thin carbon layer (Cu/C) by high-temperature pyrolysis of a self-sacrificial porous template, metal–organic framework (MOF), namely, HKUST.[21] The Cu nanoparticle-loaded GDEs were chemically modified with metallic Ag by a redox replacement process in $AgNO_3$ solution (Scheme 1a). The electroless growth of AgNPs, directly on GDEs, was controlled by varying the deposition duration. The process did not require any template, nor surfactant, or any external capping agent. Hence, it creates a clean surface for the subsequent analysis of the complex CO_2RR process. An optimum Cu/Ag composition exhibiting Cu and Ag nanoparticles with sizes in a similar range showed the highest Faradaic efficiency (FE) for CO_2 conversion products (~21% C_{2+} products, where $C_{2+} = C_2H_4$, C_2H_6, C_2H_5OH, C_3H_7OH, together with ~40% FE of HCO_2H production; Scheme 1b). In-situ Raman spectroscopy revealed the nature of the key intermediates and their binding modes to the metal surface, providing detailed mechanistic insight into the cascade mode of operation of this bimetallic Cu/Ag catalyst.

Results and Discussion

The Cu-based catalyst was synthesized by pyrolysis of a Cu MOF, namely HKUST as a self-sacrificial porous template,[21] which is composed of Cu metal centres and 1,3,5-benzenetri-carboxilic acid (H_3BTC) as organic linker, in H_2/Ar atmosphere at 800 °C. HKUST derived catalyst (HKUST@800) was characterized by powder X-ray diffraction (PXRD; Figures S1 and S2). The

sharp Bragg reflexes suggest that both MOF and the derived HKUST@800 were highly crystalline pure phases. In HKUST@800 PXRD data, reflexes at 2θ of 43.5°, 50.7°, and 74.7° were due to the formation of cubic $Fm3m$ Cu^0 phase (COD#9013015). The SEM images in Figures 1a and b show that the octahedral morphology of HKUST crystals (size of ~60±20 μm) was well preserved as a template even after the long-term carbonization process (size of ~15±5 μm); this is consistent with results from literature.[22,23] A higher magnification view of one of these octahedral microparticles revealed that each octahedron micro-particle consisted of ~80±20 nm spherically shaped CuNPs (Figures 1c and S3). A more detailed investigation of the structural properties was performed by transmission electron microscopy (TEM) to characterize the composition of individual CuNPs. The CuNPs were wrapped in thin carbon layers of ~2 to 3 nm (referred here to as Cu/C NP), and the arrangement of periodic lattice fringes with d-spacing values of 0.201 nm corresponds to the (111) planes of cubic metallic Cu^0 (Figures 1d and S4).[24] In the elemental color mapping images, Cu was predominantly present, in addition to C and a small amount of O (Figures 1d–h). The presence of 92.7 wt% of Cu was quantified using inductively coupled plasma mass spectrometry (ICP-MS) measurements. The C content in the catalyst
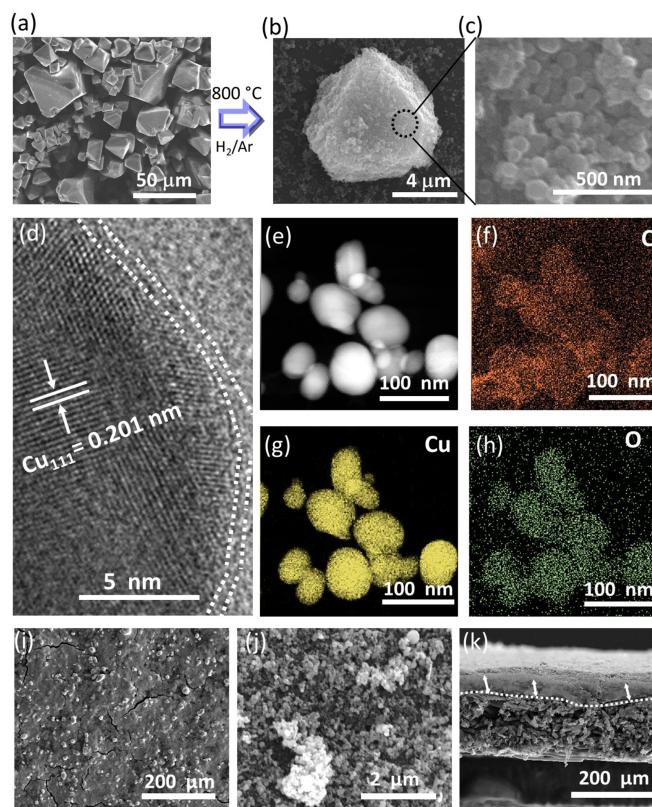
Figure 1. SEM images of a) as-synthesized HKUST crystals; b) a pyrolyzed octahedron microparticle showing a porous surface; c) a magnification of a selected area from b). d) HRTEM image of a representative particle showing the CuNP with a thin C layer. e—)–h) Elemental color mapping EDX-TEM images, showing the presence of C, Cu and O. i—)–j) HKUST@800 deposited on a GDE before electrocatalysis with different magnification and k) a cross-section SEM micrograph of the same GDE.

Scheme 1. a) Schematic of the redox replacement process of Ag on Cu/C NP. b) Cu/C and AgNPs on the gas diffusion layer (GDL) of a GDE performing electrochemical conversion of CO_2RR to gas (G) and liquid (L) products. The gaseous products are ethylene (C_2H_4), ethane (C_2H_6), and the liquid products are formic acid (HCO_2H), ethanol (C_2H_5OH) and propanol (C_3H_7OH).

Chemistry–A European Journal

Research Article
doi.org/10.1002/chem.202104249

Chemistry Europe
European Chemical
Societies Publishing

was quantified to be 3.4 wt% through elemental analysis. The N_2 adsorption isotherm (at 77 K) of HKUST@800 exhibited a type-III adsorption profile with a low N_2 uptake of ~24 $cm^3 g^{-1}$, thus suggesting a nonporous nature of the catalyst. This can be attributed to the absence of a large carbon matrix, which generally contributes to micro/macroporosity during pyrolysis (Figure S5).[23]

Before carrying out the redox replacement with Ag, HKUST@800 was first drop-coated on GDEs with an average mass loading of ~1 $mg cm^{-2}$. Figures 1i–k show a typical GDE surface covered with HKUST@800 containing only Cu/C NP (Ag@Cu/C-0). The octahedral microparticles disintegrated into nanoparticles during catalyst ink preparation due to ultra-sonication, most likely due to the low carbon content obtained upon pyrolysis.[23] Figure 1k shows the average thickness of a representative GDE to be ~45±15 μm. Ag modification was performed directly on the Cu/C modified GDE by spontaneous electroless redox replacement reaction of Ag^+ using 0.5 mM $AgNO_3$ solution at 50°C. A series of catalysts, Ag@Cu/C-0, Ag@Cu/C-3, Ag@Cu/C-7, Ag@Cu/C-15, Ag@Cu/C-24 and Ag@Cu/C-34 was prepared and characterized, where 0, 3, 7, 15, 24 and 34 denote the duration (in minutes) of the redox replacement reaction on GDEs (Figure 2). SEM investigation of the GDE surfaces displays a gradual increase in Ag nanoparticle deposition on the Cu/C surface (Figures 2a–e). Ag@Cu/C-3 and Ag@Cu/C-7 had the lowest Ag content with a non-homogeneous flaky morphology over the entire surface. Keeping the Cu/C-modified GDE in the $AgNO_3$ for 15 min (Ag@Cu/C-15), the flaky morphology of the Ag deposits turns into spherically shaped nanoparticles with sizes of ~150±50 nm. With further
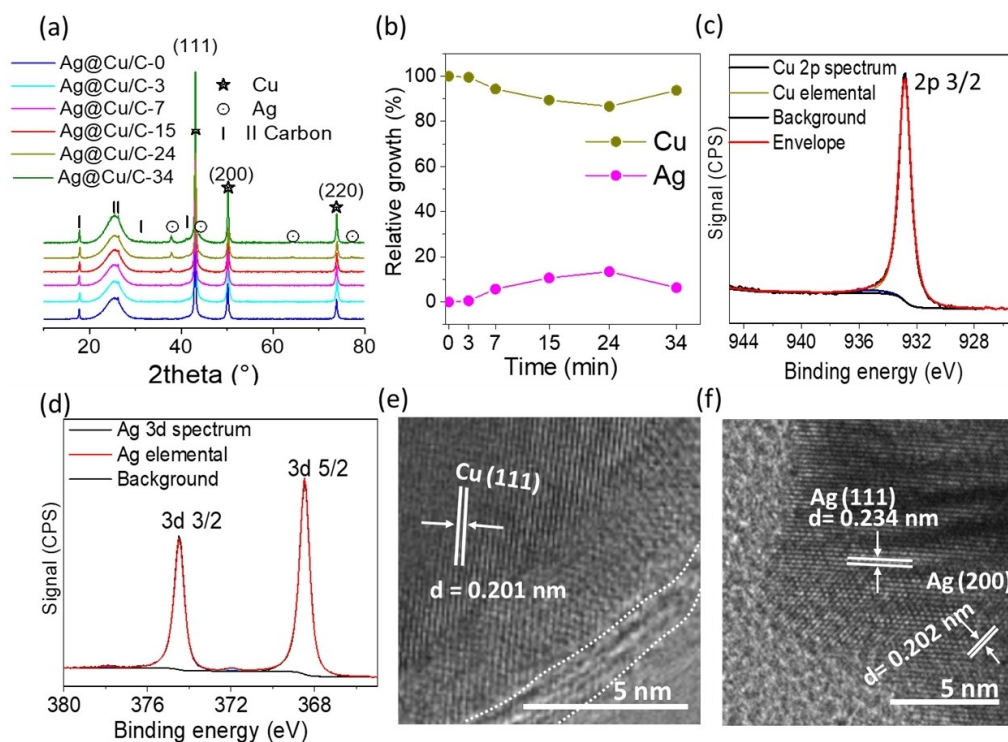
increasing reaction time until 24 (Ag@Cu/C-24) and 34 min (Ag@Cu/C-34), the sizes of the spherical particles increased to ~300±100 and ~500±100 nm, respectively (Figure S6).

SEM-EDX analysis showed homogeneous growth up to reaction times of 24 min in Ag@Cu/C-24, while heterogeneity with local agglomeration was observed for Ag@Cu/C-34. This suggests that the reduced Ag^0 is preferably deposited on already grown Ag^0 surfaces rather than seeding on Cu/C NP.

PXRD measurements with these GDEs showed a gradual increase in characteristic cubic $Fm3m$ Ag^0 (COD#9013048) peak intensities (at 37.8°, 64.3°, and 77.1°), suggesting crystalline metallic Ag deposition on the Cu/C-modified GDE surfaces (Figure 3a). Also, the prominent metallic Cu^0 reflexes indicated perseverance of crystallinity even after chemical modification. ICP-MS measurements were performed to quantify the relative loading with Cu/Ag by complete dissolution of the GDEs with acid. The Ag loadings for the different GDEs are as follows: Ag@Cu/C-3 = 0.5%, Ag@Cu/C-7 = 5.7%, Ag@Cu/C-15 = 10.6%, Ag@Cu/C-24 = 13.4%, and Ag@Cu/C-34 = 6.3% with respect to the Cu content (Figure 3b). Within the core level Cu $2p_{3/2}$ XPS spectrum of as-prepared HKUST@800, the main deconvoluted peak at 932.7 eV corresponds to metallic Cu^0 (Figure S7), also agreeing with the PXRD data shown in Figure 3a.[25] The broad C 1s spectrum was deconvoluted into C–C (284.8 eV), C=C (284.4 eV), C–O (286.2 eV), C=O (287.6 eV), and O=C=O (288.9 eV; Figure S7).[26] The XPS spectra of the Ag@Cu/C-3 to Ag@Cu/C-24 GDEs were also deconvoluted into elemental Cu^0 (core level Cu $2p_{3/2}$, binding energy 932.6±0.2 eV; Figures 3c, d and S8). The Ag@Cu/C-34 GDE revealed an additional Cu^I component, also supported by Cu LMM Auger spectra. This
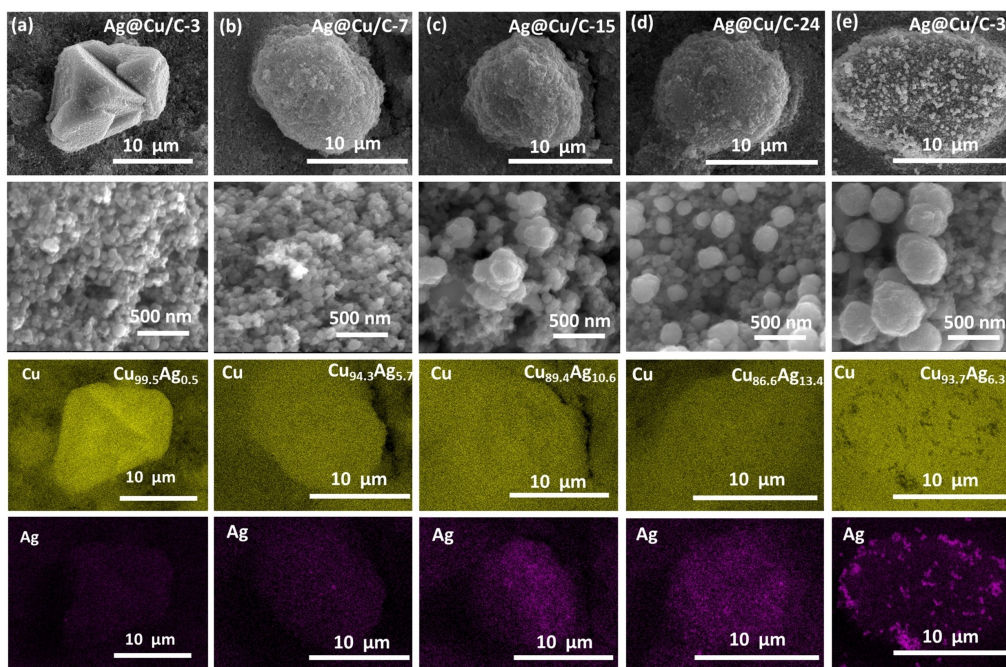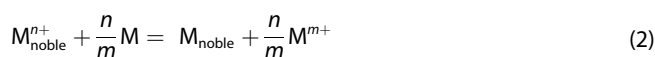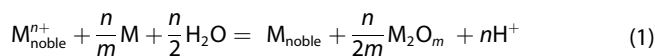

Figure 2. SEM images of Ag modified a) Ag@Cu/C-3, b) Ag@Cu/C-7, c) Ag@Cu/C-15, d) Ag@Cu/C-24 and e) Ag@Cu/C-34 GDE surfaces showing different stages of Ag deposition on Cu/C-coated GDE by means of redox replacement. Elemental colour mapping images reveal the relative increase in colour contrast of Ag with increasing deposition time, the subscript values on Cu, Ag represents the relative loading [%] of Cu/Ag in each GDE as determined by ICP-MS.

Chemistry–A European Journal

Research Article
doi.org/10.1002/chem.202104249

Chemistry Europe
European Chemical
Societies Publishing

Figure 3. a) PXRD of the Ag-modified GDEs. b) Relative Cu/Ag loading [%] determined by ICP-MS. c) and d) XPS: deconvoluted $2p_{3/2}$ core level peak of Cu and $3d$ core level peak of Ag of Ag@Cu/C-15. HRTEM images of e) Cu/C and f) AgNP in Ag@Cu/C-15, showing lattice fringes with respective d-lattice spacing values of crystal planes.

suggests that for long immersion times of the GDE into $AgNO_3$ solution, the Cu^0 tends to be oxidized to Cu^I, however, in a noncrystalline form as it was invisible in the PXRD pattern. The core level Ag $3d_{5/2}$ peak at 968.3 ± 0.3 eV was assigned to metallic Ag^0, while the same Ag^0 metallic state was also detected from PXRD (Figures 3a and S8).[27] During the redox replacement process, the less noble metal can also get oxidized and re-deposit (known as galvanic deposition), following Equation (1),[28] which can explain the formation of Cu^I phase in Ag@Cu/C-34 GDE.

$$M_{noble}^{n+} + \frac{n}{m}M + \frac{n}{2}H_2O = M_{noble} + \frac{n}{2m}M_2O_m + nH^+ \quad (1)$$

$$M_{noble}^{n+} + \frac{n}{m}M = M_{noble} + \frac{n}{m}M^{m+} \quad (2)$$

Ag@Cu/C-15 and Ag@Cu/C-24 were selected for TEM characterizations after scraping them off the GDE (Figures 3e—f and S9).

More detailed TEM images and elemental mappings of a grown Ag nanoparticle (from Ag@Cu/C-15) are shown in Figures S9a—d, indicating a cluster of smaller nanoparticles. The white perimeter lines in Figure S9d around the particles represent the AgNPs, CuNPs are located on top of AgNP. High-resolution TEM (HRTEM) images of Ag@Cu/C-15 and Ag@Cu/C-24 also support the persistence of crystalline Cu^0 and Ag^0

phases, having prominent lattice fringes with d-lattice spacing values of 0.201 nm ($Cu_{d(111)}$) and 0.234 nm ($Ag_{d(111)}$), 0.202 nm ($Ag_{d(200)}$), respectively (Figures 3e, f and S9e, f).

After redox modification with AgNP, a hydrophobic binder PTFE (see the Experimental Section, preparation of GDEs) was added on top to increase the surface hydrophobicity. Figures S10—S12 show typical surface and cross-sectional views of Ag@Cu/C-0 and Ag@Cu/C-15 (here, representative), showing the PTFE particle distribution on the Cu/C surface. The average cross-section thickness of the GDE of Ag@Cu—C-0 and Ag@Cu/C-15 is 40 ± 20 μm. After PTFE addition, no distinguishable changes on the catalyst + PTFE layer thickness were observed.

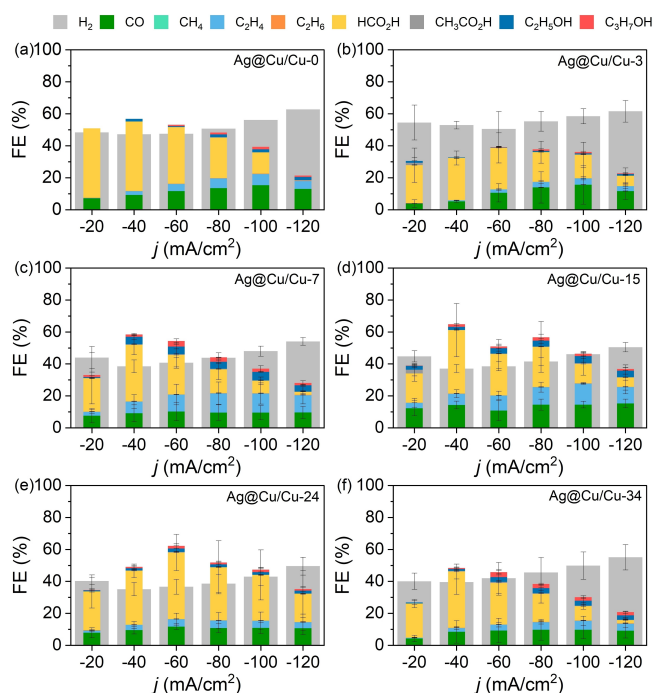## Electrochemical CO_2 reduction reaction

The CO_2 electroreduction activity of the Ag-modified catalysts, namely Ag@Cu/C-3, Ag@Cu/C-7, Ag@Cu/C-15, Ag@Cu/C-24 and Ag@Cu/C-34, were measured under steady-state conditions by performing constant-current electrolysis in 1 M KOH as the electrolyte in a custom made three-compartment GDE glass cell under constant CO_2 flow (Scheme S2). Carbon-based GDEs (see the Experimental Section) were used to fabricate the electrodes to substantially promote the CO_2 conversion rate due to improved mass transport into the three-phase boundary.[29] The measurements were performed with a set of six successive current densities (j) from -20 to -120 mA cm^{-2} using incre-

Chemistry–A European Journal

Research Article
doi.org/10.1002/chem.202104249

**Chemistry
Europe**
European Chemical
Societies Publishing

ments of -20 mA cm^{-2} (each current was applied for 870 s followed by galvanostatic impedance spectroscopy at the same current for 30 s; Figures 4 and S13). The product analysis in the absence of the Ag modification, Ag@Cu/C-0, was dominated by the presence of HCO$_2$H (FE$=43\%$) mainly at lower current densities of -20 to -40 mA cm^{-2} and H$_2$ as the second major product. The formation of CO increased up to 15% at higher current densities along with a decrease in the FE for HCO$_2$H down to 13% at -100 mA cm^{-2} (Figure 4a). In Ag@Cu/C-3, no significant change in product conversion was observed, and HCO$_2$H was the main CO$_2$RR product with a FE of 24 to 6.5% from -20 to -120 mA cm^{-2}. This is most likely due to the very small amount of Ag deposited on the Cu surface, being incapable of providing enough CO to increase the C$_{2+}$ product selectivity (Figure 4b). In the case of Ag@Cu/C-7, the overall FE values of CO were smaller compared to Ag@Cu/C-0 and Ag@Cu/C-3, respectively. Simultaneously, an increase in the conversion towards C$_{2+}$ products (C$_{2+}$=C$_2$H$_4$, C$_2$H$_6$, C$_2$H$_5$OH, C$_3$H$_7$OH) was observed (Figures 4c and S14a). The Ag@Cu/C-15 GDE led to increased production of CO compared to Ag@Cu/C-7, and the C$_{2+}$ products reached similar FE values at higher applied currents of -100 and -120 mA cm^{-2} (Figures 4d and S14a). In the case of Ag@Cu/C-24 and Ag@Cu/C-34, the conversion of C$_{2+}$ products did not further increase (Figures 4e, f and S14a). A Ag loading of ~ 5.7 to 10.6% seems to be optimal for a maximum conversion of CO$_2$ to C$_{2+}$ products (Figure S15). When the ratio of CO$_2$ converted products and H$_2$ was calculated, the values of Ag@Cu/C-15 and Ag@Cu/C-24 were comparable over the entire range of applied currents (Table S1 and Figure S14b). A correlation between higher C$_{2+}$ products and low H$_2$ formation points towards a clear impact of the increased surface-bound *CO coverage and decreased HER.[7] The higher activity towards C$_{2+}$ formation observed for Ag@Cu/C-7 and Ag@Cu/C-15 suggests that critical Ag particle sizes between $\sim 55\pm 20$ to 150 ± 50 nm are preferable, which is in a close range compared to the $\sim 80\pm 20$ nm sizes of Cu/C NP. Ag/CuNPs in a comparable size range are more feasible to steer the selectivity towards C$_{2+}$ products. Higher Ag loadings (e.g., in Ag@Cu/C-34) led to the growth of larger sized nanoparticles. In general, for all GDEs HCO$_2$H formation was observed, and the corresponding FE values were larger at low current densities between -20 to -60 mA cm^{-2} and decreased at -80 to -120 mA cm^{-2} (Figure S14c). After Ag modification, the FE values of HCO$_2$H were lower compared to unmodified Ag@Cu/C-0, and the decreasing trend of the FE for HCO$_2$H from -20 to -120 mA cm^{-2} can be explained based on the high local OH$^-$ ions activities in the vicinity of GDEs at higher current densities as HCO$_2$H formation reported to be pH dependent.[30] For the post-electrocatalysis characterization using SEM, TEM and PXRD, Ag@Cu/C-15 GDE was chosen as the representative electrode. SEM and TEM images show the formation of branched nanowires and agglomerated irregular shaped microclusters on the GDE surface (Figures S16—S19).
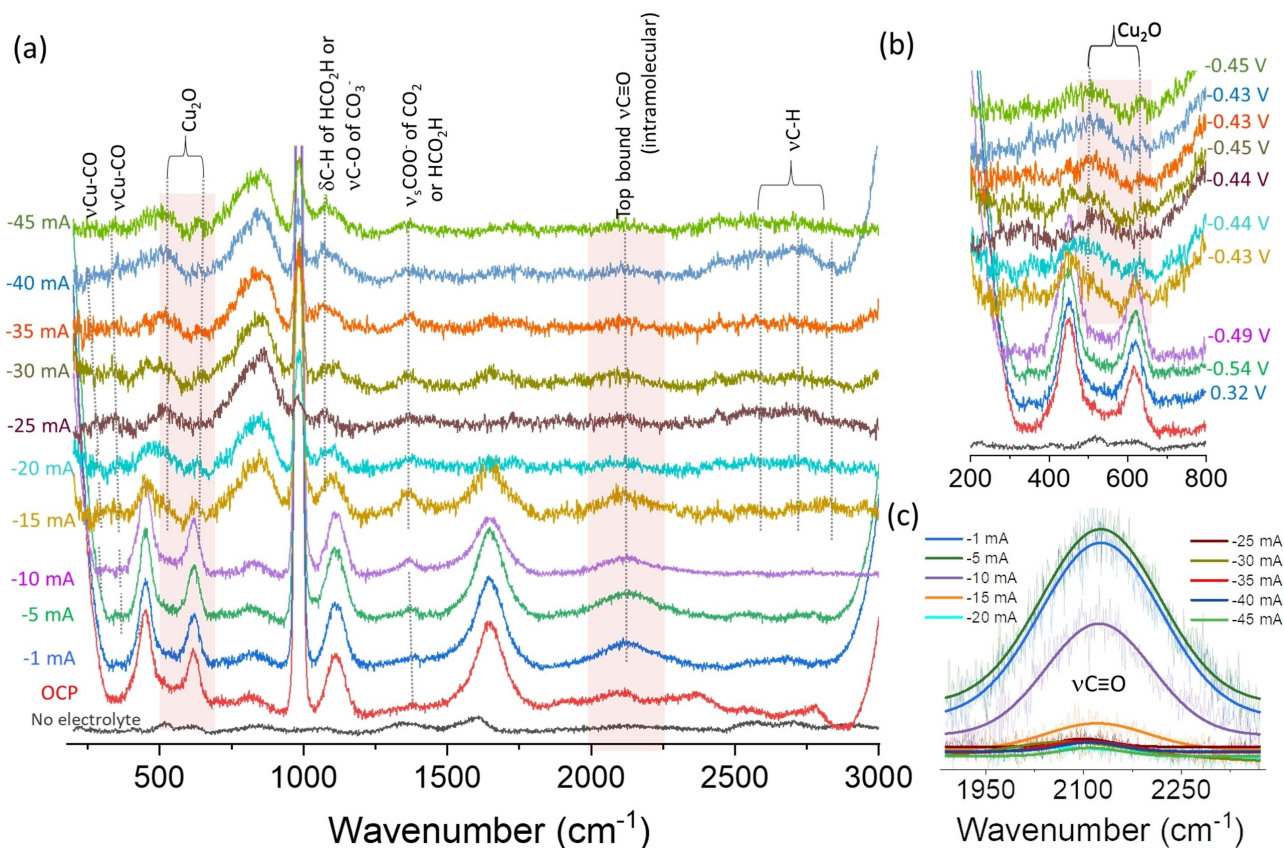
Elemental mapping of the microclusters at different magnifications revealed Cu/Ag agglomeration. Cu is known to degrade and restructure during CO$_2$ electrolysis.[5,31] The additional presence of Ag could also facilitate exposure of Cu to CO, which recently has been reported to be an accelerating Cu dissolution factor.[5] However, the crystallinity of the Cu/AgNP remained intact. In the majority of the particles, the calculated d-lattice spacing values in HRTEM images revealed the coexistence of metallic Cu and Cu$_2$O phases on the same particle (Figure S19) while the d-lattice spacing values for AgNP suggest a metallic Ag^0 phase. The cross-sectional view of the GDE did not show changes in the thickness of the catalyst layer, which is about $\sim 40\pm 15$ µm (Figure S20). The presence of K is probably from KOH or K$_2$CO$_3$/KHCO$_3$. In PXRD (Figure S21), the existence of crystalline KHCO$_3$ peaks (COD#9014545) on the same GDE hints on the formation of KHCO$_3$ due to CO$_2$ diffusion into the KOH electrolyte during electrocatalysis. Bragg reflexes of metallic Cu (COD#9013015), Ag (COD#9013048), and Cu$_2$O (COD#9005769) suggest the coexistence of mixed-valent Cu^0/Cu^I states in addition to Ag^0. Notably, the mixed-valence Cu^I/Cu^0 states act as active sites for C$_{2+}$ formation,[23,32] and the spillover of primarily formed CO from the active Ag site to the mixed-valent Cu^0/Cu^I centres enables more C$_{2+}$ formation via a cascade pathway.

In-situ Raman measurements

Ag@Cu/C-15 was chosen as a representative GDE for in-situ Raman measurements to understand the tandem effect of the Cu/Ag couple due to possible changes of the catalyst at different applied potentials, identification of catalyst-bound intermediates/products, and ultimately to monitor the active state of the catalyst during the electrochemical reaction (Figure 5). We used KOH as the electrolyte in the gas diffusion

Figure 4. FE [%] for all CO$_2$RR products vs. applied current density (j [mA cm^{-2}]) as obtained from Ag-modified and unmodified GDEs.

Chem. Eur. J. **2022**, 28, e202104249 (5 of 9)

© 2022 The Authors. Chemistry - A European Journal published by Wiley-VCH GmbH

Chemistry–A European Journal

Research Article
doi.org/10.1002/chem.202104249

**Chemistry
Europe**
European Chemical
Societies Publishing

Figure 5. a) In-situ Raman measurements in 0.01 M KOH + 0.6 M K_2SO_4 electrolyte solution under constant CO_2 flow; from the bottom −1 to −10 mA: y-axis multiplication factor 20, from −15 to −45 mA: y-axis multiplication factor 100. b) Magnified lower wavenumber [cm^{-1}] x-axis showing the generation of Cu_2O peaks, the potential values are iR-corrected and in RHE. c) X-axis in the area of top bound linear CO generation with applied current [mA], working electrode (WE) surface area: 2.01 cm^2. The spectra being noisy, were fitted into Gaussian.

cell where CO_2 was continuously flowing (~20 mL min^{-1}) towards the bottom of the GDE (Scheme S3), although the majority of reported in-situ studies were performed in KHCO$_3$.[13−19] It is one of the advantages of GDEs that the gaseous CO_2 is separated from the electrolyte and hence CO_3^{2-} formation is suppressed while the competing HER is additionally suppressed at higher pH values. Hence the GDE is offering the opportunity to improve the CO_2 mass transport to the catalyst's active sites, avoiding CO_3^{2-} formation and simultaneously suppress the HER. To emulate the conditions used during the GC-coupled electrochemical measurements, we used diluted KOH for the in-situ Raman spectroscopy. Each spectrum was recorded at a constant current in 0.01 M KOH to maintain the pH at ~12 in the set-up, which is necessary as the immersible objective does not withstand higher pH values. To adjust the ionic strength of the electrolyte and to improve the conductivity of the KOH solution, K_2SO_4 was added as supporting electrolyte, while other potassium salts such as KNO_3, KCl, KBr, KI, etc. were deliberately avoided to cancel out the possible interference in the CO_2RR reaction.[33] Each current was applied for 300 s at the GDE, and Raman spectra were recorded within that time frame at a constant CO_2 flow. The Raman bands at 450, 616, 983, 1112 cm^{-1} at OCP are due to the presence of K_2SO_4 (Figure 5a).[34] The broad band with varying intensity at 1645 cm^{-1} is

caused by the bending mode of the H–O–H vibration (δ_{HOH}) from surface adsorbed interfacial water molecules.[14] A weak band at 1380 cm^{-1} is due to the CO_2 vibration mode.[15,16] Even at small applied currents, for example of −1 and −5 mA, a weak band appeared in the lower wavenumber region at 348 cm^{-1}, corresponding to Cu–CO stretch vibration modes (on-top geometry).[17]

Concomitantly, a strong band at 2124 cm^{-1} from linearly coordinated on-top bound $\nu C\equiv O$ (intramolecular) of the CO molecule was detected.[17,35,36] At −10 mA and higher currents, a weak intensity band started growing at 287 cm^{-1} which can be related to Cu–CO frustrated rotation (on-top geometry),[17] strongly suggesting metal-bound CO formation during electrocatalysis, with a minor frequency shift of ±10 cm^{-1} with increasing applied current which is supposedly due to a vibrational Stark tuning effect.[18] The increase in the relative intensity of the vibration mode at 1380 cm^{-1} could be a contribution from both CO_2 and the formation of $\nu_s COO^-$ of deprotonated HCO_2H (as the electrolyte is alkaline). If HCO_2H was formed together with intermediate CO, another strong mode of $\nu_{as} COO^-$ is supposed to be present in the range of 1620 to 1660 cm^{-1}; however, these bands are masked by the δ_{HOH} mode. At −15 mA, a growing shoulder at 531 cm^{-1} and a band at 627 cm^{-1} could be accounted for Cu_2O.[17,37] Although

Chem. Eur. J. **2022**, *28*, e202104249 (6 of 9)

© 2022 The Authors. Chemistry - A European Journal published by Wiley-VCH GmbH

Chemistry–A European Journal

Research Article
doi.org/10.1002/chem.202104249

Chemistry Europe
European Chemical
Societies Publishing

the band at 627 cm^{-1} merged with the K$_2$SO$_4$ band initially, they were distinguishable in the Raman spectra recorded at higher currents. A small response in the region of 2600 to 2900 cm^{-1} was observed, corresponding to νC–H vibrations.[36] With increasing currents from −20 mA onwards, the bands at 531 and 627 cm^{-1} for Cu$_2$O became prominently visible, suggesting the formation of Cu^I species during the CO$_2$RR (Figure 5b).[38] The growing shoulder at 1075 cm^{-1} could be a contribution from ν_sC–O stretching modes of carbonate or δ_{as}C–H of HCO$_2$H.[39] The intensity of on-top bound CO at 2124 cm^{-1} decreased; however, the relative intensity in the region of 2600 to 2900 cm^{-1} was preserved (Figure 5c). The presence of small bands with low intensity in the lower wavenumber region at 287 and 348 cm^{-1} confirms the presence of metal–CO bonds attached to the surface. Together with the decrease in the CO signal intensity at 2124 cm^{-1} and concomitant increase of bands at 2600 to 2900 cm^{-1}, it is supposed that CO was consumed or re-adsorbed and converted to higher hydrocarbon C$_{2+}$ products via a cascade pathway. The low intensity of C–H bands can be explained by the fact of low overall C$_{2+}$ products conversion. The signal-to-noise ratio in the recorded spectra at higher currents can be correlated to vigorous gas bubble formation (mainly due to HER) with increasing applied current. When the potential values were corrected by the uncompensated solution resistance (R_u), the CO peak was detected at potential values between 0.32 and −0.44 V (vs. RHE); however, the peak intensity decreased with higher currents. In agreement with the electrolysis with coupled gas chromatography (Figure S22) also the Raman data suggest maximum products formation in the potential range of −0.28 and −0.40 V. Hence, it can be anticipated that this potential range is optimal for the cascade reaction at the Cu/Ag-modified GDE surface. The formation of HCO$_2$H or related intermediates (formyoxyl or carboxyl, metal-bound OC species)[35] was inconclusive due to overlapping bands in the region of CO$_2$ or carbonate vibrations. However, the HPLC results confirm HCO$_2$H formation. Hence, simultaneous operation of two reaction pathways under the formation of C–C-coupled products and HCO$_2$H on bimetallic Cu/C–Ag surface can be concluded.

Conclusion

A novel Cu/C–Ag nanostructured catalyst has been synthesized by means of a redox replacement process, in which the relative ratio of both metals can be tuned by the reaction time. GC, HPLC and Raman spectroscopy suggest that cascade reactions proceed on Ag-modified Cu/C surfaces. As-prepared Cu/C NPs were predominantly selective towards H$_2$ and HCO$_2$H; however, once treated with Ag, the selectivity towards C$_{2+}$ products improved significantly. The presence of AgNPs on top, preferably at a comparable size to the CuNPs, contributed to the formation of CO and hence to improving C–C coupling reactions under formation of C$_{2+}$ products. In-situ Raman measurements in a gas diffusion cell revealed the formation of on-top bound linear CO at low overpotentials, which is consumed at higher currents. The appearance of νCu–CO

vibration modes suggests the continuous formation of metal-bound linear CO; which is converted into C–C-coupled products, as also supported by growing νC–H bands. Cu$_2$O formation throughout the measurements implied the generation of Cu^I species as active intermediates for CO$_2$RR. The results from GC, HPLC, and Raman spectroscopy indicate the parallel operation of two competitive mechanisms towards the production of HCO$_2$H and C–C-coupled products on Cu/Ag bimetallic surfaces.

Experimental Section

Preparation of gas-diffusion electrodes (GDEs): The working electrodes are commercial GDEs (Freudenberg H23C2) with a carbon paper gas diffusion layer (GDL) covered with a microporous layer (MPL); diameter: 2.4 cm, effective working electrode diameter 1.7 cm). It was modified with HKUST@800 at a mass loading of 1 mg cm^{-2} by drop casting. ~5 mg of catalyst powders were suspended in EtOH (1 mL), and ultrasonicated for 30 min, maintaining the temperature of the water bath always at or below room temperature (adjusted with ice cubes). The catalyst ink was slowly transferred to the GDE by drop-casting and drying under ambient conditions overnight.

Next, the redox replacement reaction was carried out in 0.5 mM AgNO$_3$ solution at 50 °C. ~46 mL AgNO$_3$ solution is filled into a beaker. The temperature was maintained by immersing the beaker in a water bath (Scheme S1), which was continuously stirred during the whole experiment. The GDEs were dipped into the AgNO$_3$ solution for 0 (Ag@Cu/C-0), 3 (Ag@Cu/C-3), 7 (Ag@Cu/C-7), 15 (Ag@Cu/C-15), 24 (Ag@Cu/C-24) and 34 min (Ag@Cu/C-34) to attain a specific Ag mass loading on the Cu/C NPs. After taking the modified GDEs out from the AgNO$_3$ solution, the backside of the GDEs were washed slowly with water/EtOH (3:1, v/v). The front side was washed several times with water to remove loosely bound Ag from the surface. The GDEs were dried at ambient conditions overnight. After drying, PTFE in EtOH solution (10 wt% with respect to ~1 mg cm^{-2} catalyst loading) was prepared and added on top of each GDE. PTFE-modified GDEs were only used for electrochemical experiments. For the characterization, as-prepared Ag-modified GDEs were used without PTFE addition unless otherwise mentioned.

Electrochemical measurements: A custom-made three-compartment glass electrochemical cell was used. The cell has two compartments separated by an anion exchange membrane (AEM, FAB-PK-75, Fumatech; Scheme S2). The anode compartment was equipped with the counter electrode (Ni foam) and the cathode compartment was equipped with the reference (double junction Ag|AgCl/3 M KCl) and the working electrode (GDE). CO$_2$ was constantly supplied from the backside to the GDE through the gas feed chamber. Before the measurement, the anode and cathode compartments were filled with 14 and 15 mL 1 M KOH as electrolyte, respectively. Chronopotentiometry for 870 s was performed followed by a 30 s galvanostatic EIS measurement at six different currents. During the measurements, two mass flow controllers (MFCs, AALBORG) were used to set a flow for N$_2$ (16 mL min^{-1}) to constantly purge the catholyte carrying the gaseous products to the GC while excluding contamination with O$_2$ in the electrolyte, and for CO$_2$ (20 mL min^{-1}). Two outlets of the reactor were connected to a 6-way valve, allowing to switch between the gaseous products evolved from the GDE (*headspace* products) and the products in the CO$_2$ chamber (*gas feed compartment*) and at the same time maintaining a specific CO$_2$ back pressure. The value of the applied potential values (vs. Ag/AgCl) was converted to the

Chemistry–A European Journal

Research Article
doi.org/10.1002/chem.202104249

Chemistry Europe
European Chemical
Societies Publishing

scale of the reversible hydrogen electrode (RHE) using the following equation considering the electrolyte bulk pH of 1 M KOH solution equal to 13.9: $E_{RHE} = E_{Ag|AgCl (3 M KCl)} + 0.210 + (0.059 \, pH)$. All potential values were further iR corrected. In the galvanostatic EIS, the applied current varied from -20 to $-120 \, mA \, cm^{-2}$ (-45.2 to $-271 \, mA$, considering a geometric surface area of $2.27 \, cm^2$ of the working electrode). The intensity of the current perturbation was always 10% of the applied current, for example, at $-20 \, mA \, cm^{-2}$ ($-45.2 \, mA$) applied current, the perturbation was $-2 \, mA \, cm^{-2}$ ($-4.52 \, mA$). A representative galvanostatic EIS is provided in Figure S13 for better clarity of the experimental conditions.

In-situ Raman experiments: In-situ Raman measurements were carried out with the aforementioned Raman spectrometer equipped with an immersible 60× objective (Zeiss). The objective was immersed into the electrolyte in an in-house developed electrochemical cell consisting of a polytetrafluoroethylene cell body mounted on the catalytically active Ag@Cu/C-15 (Scheme S3). The cell was sealed using a tightly pressed O-ring to prevent electrolyte leakage. The measurements were performed in 0.01 M KOH + 0.6 M K_2SO_4 solution (Ar purged before adding into cell) with a Pt mesh as CE and a Ag/AgCl/3 M KCl as RE. The pH of the electrolyte was ~12. The GDE was connected as the WE to an Autolab potentiostat. Each current was applied for 300 s. Raman spectra were recorded using a grating of 1200 grooves mm^{-1}, an exposure time of 5 s, and three repetitions under illumination with a 532 nm laser.

Conflict of Interest

The authors declare no conflict of interest.

Data Availability Statement

The data that support the findings of this study are available from the corresponding author upon reasonable request.

Keywords: cascade reactions · CO$_2$ reduction · electrocatalysis · in-situ Raman spectroscopy · redox replacement

[1] a) Y. Hori, A. Murata, R. Takahashi, *J. Chem. Soc. Faraday Trans. 1* **1989**, *85*, 2309—2326; b) Y. Hori, K. Kikuchi, A. Murata, S. Suzuki, *Chem. Lett.* **1986**, *15*, 897—898; c) M. B. Ross, P. de Luna, Y. Li, C.-T. Dinh, D. Kim, P. Yang, E. H. Sargent, *Nat. Catal.* **2019**, *2*, 648—658; d) K. P. Kuhl, E. R. Cave, D. N. Abram, T. F. Jaramillo, *Energy Environ. Sci.* **2012**, *5*, 7050—7059.

[2] a) C. Chen, J. F. Khosrowabadi Kotyk, S. W. Sheehan, *Chem* **2018**, *4*, 2571—2586; b) M. G. Kibria, J. P. Edwards, C. M. Gabardo, C.-T. Dinh, A. Seifitokaldani, D. Sinton, E. H. Sargent, *Adv. Mater.* **2019**, *31*, e1807166; c) R. Kas, K. Yang, D. Bohra, R. Kortlever, T. Burdyny, W. A. Smith, *Chem. Sci.* **2020**, *11*, 1738—1749; d) L. Fan, C. Xia, F. Yang, J. Wang, H. Wang, Y. Lu, *Sci. Adv.* **2020**, *6*, eaay3111; e) K. Junge Puring, D. Siegmund, J. Timm, F. Möllenbruck, S. Schemme, R. Marschall, U.-P. Apfel, *Adv. Sustainable Syst.* **2021**, *5*, 2000088; f) U. O. Nwabara, M. P. de Heer, E. R. Cofell, S. Verma, E. Negro, P. J. A. Kenis, *J. Mater. Chem. A* **2020**, *8*, 22557—22571; g) S. Garg, M. Li, A. Z. Weber, L. Ge, L. Li, V. Rudolph, G. Wang, T. E. Rufford, *J. Mater. Chem. A* **2020**, *8*, 1511—1544.

[3] a) A. A. Peterson, F. Abild-Pedersen, F. Studt, J. Rossmeisl, J. K. Nørskov, *Energy Environ. Sci.* **2010**, *3*, 1311—1315; b) O. Piqué, Q. H. Low, A. D. Handoko, B. S. Yeo, F. Calle-Vallejo, *Angew. Chem. Int. Ed.* **2021**, *60*, 10784—10790; *Angew. Chem.* **2021**, *133*, 10879—10885; c) Y. Y. Birdja, E. Pérez-Gallent, M. C. Figueiredo, A. J. Göttle, F. Calle-Vallejo, M. T. M. Koper, *Nat. Energy* **2019**, *4*, 732—745; d) A. Vasileff, C. Xu, Y. Jiao, Y. Zheng, S.-Z. Qiao, *Chem* **2018**, *4*, 1809—1831.

[4] a) C. G. Morales-Guio, E. R. Cave, S. A. Nitopi, J. T. Feaster, L. Wang, K. P. Kuhl, A. Jackson, N. C. Johnson, D. N. Abram, T. Hatsukade, C. Hahn, T. F. Jaramillo, *Nat. Catal.* **2018**, *1*, 764—771; b) L. Lin, T. Liu, J. Xiao, H. Li, P. Wie, D. Gao, B. Nan, R. Si, G. Wang, X. Bao, *Angew. Chem. Int. Ed.* **2020**, *59*, 2240—8—22413; *Angew. Chem.* **2020**, *132*, 225—4—22599; c) H. Zhang, X. Chang, J. G. Chen, W. A. Goddard, B. Xu, M.-J. Cheng, Q. Lu, *Nat. Commun.* **2019**, *10*, 3340; d) L. Castilla-Amorós, D. Stoian, J. R. Pankhurst, S. B. Varandili, R. Buonsanti, *J. Am. Chem. Soc.* **2020**, *142*, 1928—3—19290; e) Y. Wang, L. Cao, N. J. Libretto, X. Li, C. Li, Y. Wan, C. He, J. Lee, J. Gregg, H. Zong, D. Su, J. T. Miller, T. Mueller, C. Wang, *J. Am. Chem. Soc.* **2019**, *141*, 1663—5—16642; f) W. Ren, X. Tan, J. Qu, S. Li, J. Li, X. Liu, S. P. Ringer, J. M. Cairney, K. Wang, S. C. Smith, C. Zhao, *Nat. Commun.* **2021**, *12*, 1449.

[5] P. Wilde, P. B' O'Mara, J. R. C. Junqueira, T. Tarnev, T. M. Benedetti, C. Andronescu, Y.-T. Chen, R. D. Tilley, W. Schuhmann, J. J. Gooding, *Chem. Sci.* **2021**, *12*, 402—8—4033.

[6] Y. Lum, J. W. Ager, *Energy Environ. Sci.* **2018**, *11*, 293—5—2944.

[7] Y.-J. Zhang, V. Sethuraman, R. Michalsky, A. A. Peterson, *ACS Catal.* **2014**, *4*, 374—2—3748.

[8] a) P. B' O'Mara, P. Wilde, T. M. Benedetti, C. Andronescu, S. Cheong, J. J. Gooding, R. D. Tilley, W. Schuhmann, *J. Am. Chem. Soc.* **2019**, *141*, 1409—3—14097; b) J. Li, X. Chang, H. Zhang, A. S. Malkani, M.-J. Cheng, B. Xu, Q. Lu, *Nat. Commun.* **2021**, *12*, 3264; c) W. Zhang, C. Xu, Y. Hu, S. Yang, L. Ma, L. Wang, P. Zhao, C. Wang, J. Ma, Z. Jin, *Nano Energy* **2020**, *73*, 104796; d) W. Zhang, Y. Hu, L. Ma, G. Zhu, Y. Wang, X. Xue, R. Chen, S. Yang, Z. Jin, *Adv. Sci.* **2018**, *5*, 1700275.

[9] T. T. H. Hoang, S. Verma, S. Ma, T. T. Fister, J. Timoshenko, A. I. Frenkel, P. J. A. Kenis, A. A. Gewirth, *J. Am. Chem. Soc.* **2018**, *140*, 579—1—5797.

[10] E. L. Clark, C. Hahn, T. F. Jaramillo, A. T. Bell, *J. Am. Chem. Soc.* **2017**, *139*, 1584—8—15857.

[11] S. Ma, M. Sadakiyo, M. Heima, R. Luo, R. T. Haasch, J. I. Gold, M. Yamauchi, P. J. A. Kenis, *J. Am. Chem. Soc.* **2017**, *139*, 4—7—50.

[12] a) D. Higgins, A. T. Landers, Y. Ji, S. Nitopi, C. G. Morales-Guio, L. Wang, K. Chan, C. Hahn, T. F. Jaramillo, *ACS Energy Lett.* **2018**, *3*, 294—7—2955; b) P. R. Subramanian, J. H. Perepezko, *JPE* **1993**, *14*, 6—2—75.

[13] J. Gao, H. Zhang, X. Guo, J. Luo, S. M. Zakeeruddin, D. Ren, M. Grätzel, *J. Am. Chem. Soc.* **2019**, *141*, 1870—4—18714.

[14] M. Moradzaman, G. Mul, *ChemElectroChem* **2021**, *8*, 147—8—1485.

[15] K. Kneipp, Y. Wang, A. Berger, R. Dasari, M. Feld, *J. Raman Spectrosc.* **1995**, *26*, 95—9—962.

[16] A. R. Davis, B. G. Oliver, *J. Solution Chem.* **1972**, *1*, 32—9—339.

[17] S. Jiang, K. Klingan, C. Pasquini, H. Dau, *J. Chem. Phys.* **2019**, *150*, 41718.

[18] J. M. Marr, Z. D. Schultz, *J. Phys. Chem. Lett.* **2013**, *4*, 326—8—3272.

[19] A. Dutta, I. Z. Montiel, R. Erni, K. Kiran, M. Rahaman, J. Drnec, P. Broekmann, *Nano Energy* **2020**, *68*, 104331.

[20] a) S. M. Alia, Y. S. Yan, B. S. Pivovar, *Catal. Sci. Technol.* **2014**, *4*, 358—9—3600; b) Z.-Y. Chang, S.-J. Huo, J.-M. He, J.-H. Fang, *Surf. Interfaces* **2017**, *6*, 11—6—121.

[21] S. S. Chui, S. M. Lo, J. P. Charmant, A. G. Orpen, I. D. Williams, *Science* **1999**, *283*, 114—8—1150.

[22] K. Zhao, Y. Liu, X. Quan, S. Chen, H. Yu, *ACS Appl. Mater. Interfaces* **2017**, *9*, 530—2–5311.

[23] N. Sikdar, J. R. C. Junqueira, S. Dieckhöfer, T. Quast, M. Braun, Y. Song, H. B. Aiyappa, S. Seisel, J. Weidner, D. Öhl, C. Andronescu, W. Schuhmann, *Angew. Chem. Int. Ed.* **2021**, *60*, 2342—7–23434; *Angew. Chem.* **2021**, *133*, 2361—6–23624.

[24] G. Cheng, A. R. Hight Walker, *Anal. Bioanal. Chem.* **2010**, *396*, 105—7–1069.

[25] M. C. Biesinger, *Surf. Interface Anal.* **2017**, *49*, 132—5–1334.

[26] D. J. Morgan, *C* **2021**, *7*, 51.

[27] A. M. Ferraria, A. P. Carapeto, A. M. Botelho do Rego, *Vacuum* **2012**, *86*, 198—8–1991.

[28] A. Papaderakis, I. Mintsouli, J. Georgieva, S. Sotiropoulos, *Catalysts* **2017**, *7*, 80.

[29] a) M. N. Mahmood, D. Masheder, C. J. Harty, *J. Appl. Electrochem.* **1987**, *17*, 115—9–1170; b) M. Ma, E. L. Clark, K. T. Therkildsen, S. Dalsgaard, I. Chorkendorff, B. Seger, *Energy Environ. Sci.* **2020**, *13*, 97—7–985.

[30] M. König, J. Vaes, E. Klemm, D. Pant, *iScience* **2019**, *19*, 13—5–160.

[31] a) B. Eren, R. S. Weatherup, N. Liakakos, G. A. Somorjai, M. Salmeron, *J. Am. Chem. Soc.* **2016**, *138*, 820—7–8211; b) J. Huang, N. Hörmann, E. Oveisi, A. Loiudice, G. L. de Gregorio, O. Andreussi, N. Marzari, R. Buonsanti, *Nat. Commun.* **2018**, *9*, 3117; c) W. T. Osowiecki, J. J. Nussbaum, G. A. Kamat, G. Katsoukis, M. Ledendecker, H. Frei, A. T. Bell, A. P. Alivisatos, *ACS Appl. Energ. Mater.* **2019**, *2*, 774—4–7749.

[32] P.-P. Yang, X.-L. Zhang, F.-Y. Gao, Y.-R. Zheng, Z.-Z. Niu, X. Yu, R. Liu, Z.-Z. Wu, S. Qin, L.-P. Chi, Y. Duan, T. Ma, X.-S. Zheng, J.-F. Zhu, H.-J. Wang, M.-R. Gao, S.-H. Yu, *J. Am. Chem. Soc.* **2020**, *142*, 640—0–6408.

[33] a) T. Kim, G. T. R. Palmore, *Nat. Commun.* **2020**, *11*, 3622; b) X. Zhang, J. Li, Y.-Y. Li, Y. Jung, Y. Kuang, G. Zhu, Y. Liang, H. Dai, *J. Am. Chem. Soc.* **2021**, *143*, 324—5–3255.

[34] J. Qiu, X. Li, X. Qi, *IEEE Photon. J.* **2019**, *11*, —1–12.

[35] I. V. Chernyshova, P. Somasundaran, S. Ponnurangam, *Proc. Natl. Acad. Sci. USA* **2018**, *115*, E926—1–E9270.

[36] D. Öhl, Y. U. Kayran, J. R. C. Junqueira, V. Eßmann, T. Bobrowski, W. Schuhmann, *Langmuir* **2018**, *34*, 1229—3–12301.

[37] a) S. Choudhary, J. V. N. Sarma, S. Pande, S. Ababou-Girard, P. Turban, B. Lepine, S. Gangopadhyay, *AIP Adv.* **2018**, *8*, 55114; b) L. Jiang, T. You, P. Yin, Y. Shang, D. Zhang, L. Guo, S. Yang, *Nanoscale* **2013**, *5*, 278—4–2789.

[38] a) Y. Song, J. R. C. Junqueira, N. Sikdar, D. Öhl, S. Dieckhöfer, T. Quast, S. Seisel, J. Masa, C. Andronescu, W. Schuhmann, *Angew. Chem. Int. Ed.* **2021**, *60*, 913—5–9141; *Angew. Chem.* **2021**, *133*, 921—7–9224; b) L. Mandal, K. R. Yang, M. R. Motapothula, D. Ren, P. Lobaccaro, A. Patra, M. Sherburne, V. S. Batista, B. S. Yeo, J. W. Ager, J. Martin, T. Venkatesan, *ACS Appl. Mater. Interfaces* **2018**, *10*, 857—4–8584.

[39] H. Jeziorowski, B. Moser, *Mikrochim. Acta* **1989**, *98*, 10—1–107.